Paudel, Rishi R. et al. K2 Ultracool Dwarfs Survey. III. White Light Flares Are Ubiquitous in M6-L0 Dwarfs. The Astrophysical Journal 858 (May 4, 2018), no. 1. https://doi.org/10.3847/1538-4357/aab8fe.

Access to this work was provided by the University of Maryland, Baltimore County (UMBC) ScholarWorks@UMBC digital repository on the Maryland Shared Open Access (MD-SOAR) platform.

Please provide feedback

Please support the ScholarWorks@UMBC repository by emailing scholarworks-group@umbc.edu and telling us what having access to this work means to you and why it's important to you. Thank you.

K2 ULTRACOOL DWARFS SURVEY. III. WHITE LIGHT FLARES ARE UBIQUITOUS IN M6-L0 DWARFS

Rishi R. Paudel, John E. Gizis, D. J. Mullan,[1] Sarah J. Schmidt,[2] Adam J. Burgasser,[3] Peter K. G. Williams,[4]
and Edo Berger[4]

[1] *Department of Physics and Astronomy, University of Delaware, Newark, DE, 19716, USA*

[2] *Leibniz-Institute for Astrophysics Potsdam (AIP), An der Sternwarte 16, 14482, Potsdam, Germany*

[3] *Center for Astrophysics and Space Science, University of California San Diego, La Jolla, CA 92093, USA*

[4] *Harvard-Smithsonian Center for Astrophysics, 60 Garden Street, Cambridge, MA 02138, USA*

ABSTRACT

We report the white light flare rates for 10 ultracool dwarfs (UCDs) using *Kepler K2* short cadence data. Among our sample stars, two have spectral type M6, three are M7, three are M8 and two are L0. Most of our targets are old low mass stars. We identify a total of 283 flares in all of the stars in our sample, with *Kepler* energies in the range $\log E_{Kp}$ $\sim$(29 - 33.5) erg. Using the maximum-likelihood method of line fitting, we find that the flare frequency distribution (FFD) for each star in our sample follows a power law with slope -α in range -(1.3-2.0). We find that cooler objects tend to have shallower slopes. For some of our targets, the FFD follows either a broken power law, or a power law with an exponential cutoff. For the L0 dwarf 2MASS J12321827-0951502, we find a very shallow slope (-α = -1.3) in the *Kepler* energy range $(0.82\text{-}130)\times10^{30}$ erg: this L0 dwarf has flare rates which are comparable to the rates of high energy flares in stars of earlier spectral types. In addition, we report photometry of two superflares: one on the L0 dwarf 2MASS J12321827-0951502 and another on the M7 dwarf 2MASS J08352366+1029318. In case of 2MASS J12321827-0951502, we report a flare brightening by a factor of $\sim$144 relative to the quiescent photospheric level. Likewise, for 2MASS J08352366+1029318, we report a flare brightening by a factor of $\sim$60 relative to the quiescent photospheric level. These two superflares have bolometric (UV/optical/infrared) energies 3.6×10^{33} erg and 8.9×10^{33} erg respectively, while the FWHM time scales are very short, $\sim$2 minutes. We find that the M8 star TRAPPIST-1 is more active than the M8.5 dwarf: 2M03264453+1919309, but less active than another M8 dwarf (2M12215066-0843197).

1. INTRODUCTION

Ultracool dwarfs (hereafter UCDs) are stellar or substellar objects with effective temperatures no more than 2700K (Martín et al. 1999; Kirkpatrick et al. 1999). Understanding the nature of magnetic dynamos in UCDs has been very challenging. The UCDs show deviations from age, rotation and activity relations which are seen in early and mid-M dwarfs. The rotation rate plays a significant role in shaping the magnetic dynamo of early and mid-M dwarfs. When the stars are young, their rapid rotation rates empower strong magnetic dynamos. As they evolve, magnetic braking slows the rotation, which in turn decreases the magnetic activity (Donati & Landstreet 2009; Gershberg 2005; Telleschi et al. 2005). The UCDs (which include both young brown dwarfs and old low-mass stars), despite being rapid rotators, display a poor relation between rotation and magnetic activity. Some of the usual indicators of activity (X-ray and H_α emission) weaken significantly among the UCDs (Gizis et al. 2000; Berger et al. 2010; Schmidt et al. 2015). This could be due to a number of factors, including cool atmospheres which have reduced amounts of ionized gas (Mohanty et al. 2002), or atmospheres which are undergoing centrifugal coronal stripping (James et al. 2000; Jardine & Unruh 1999; Berger et al. 2008). On the other hand, observations of radio emission show that strong magnetic fields exist in UCDs (Route & Wolszczan 2012; Williams & Berger 2015; Route & Wolszczan 2016). One interpretation of these data is that turbulent dynamos in UCDs may be producing both large and small scale magnetic fields (Reiners & Christensen 2010; Yadav et al. 2015). Alternatively, X-rays and H_α emission may be powered by fast magnetic reconnection, whereas radio emission may be generated by electrons which emerge from slow magnetic reconnection (Mullan 2010).

Stellar flares are transient events which are caused by sudden releases of magnetic energy in the upper atmosphere of the star. During this process, energy which was previously stored in magnetic form is converted (by reconnection) in part to kinetic energy of electrons and ions, in part to bulk flow of ejected matter (coronal mass ejections: CMEs) (Mullan 2010; Benz & Güdel 2010), and in part to thermal energy. White light flares (hereafter WLFs) are assumed to be produced when non thermal electrons accelerated after reconnection hit a cold thick target in lower chromosphere or upper photosphere. The precipitated electrons cause the formation of hot "chromospheric condensations" which emit white light continuum: the continuum has a wavelength dependence in visible photons which approximates that of a blackbody with a temperature of order 10^4 K (Kowalski et al. (2015) and references therein). During a WLF, a faint star can become significantly brighter in optical light, by as much as several magnitudes. Two huge WLFs on UCDs will be discussed later in this paper. Estimates of surface areas of flares show that the WLFs in UCDs cover larger fractional areas of the surface than do flares on bright stars such as the Sun (Kowalski et al. 2010; Walkowicz et al. 2011). Pineda et al. (2017) suggest that flares on brown dwarfs could result from planet like auroral emissions produced by large-scale magnetospheric currents.

The discovery of the TRAPPIST-1 planetary system (Gillon et al. 2016, 2017; Luger et al. 2017) around an M8.0 dwarf suggests that more such planetary systems around other M stars or possibly brown dwarfs may be discovered. Thus, there will be increased chances of finding Earth like planets in the habitable zones (HZ) of such stars. To know the habitable conditions of such planets, it will be important to know flare rates on the host stars: UV photons from huge flares may have significant impact on the chemical evolution of the atmospheres of the planets (Segura et al. 2010; Grenfell et al. 2014; Armstrong et al. 2016; Owen & Mohanty 2016). In this regard, studies of the WLF rates of UCDs will contribute to the conclusions.

The *Kepler* mission (Koch et al. 2010) was originally aimed at finding more Earth sized planets. But it has also turned out to be useful for studying stellar properties, including WLF rates, astroseismology, etc. WLF rates of several early-M and mid-M dwarfs were estimated using *Kepler* data (Ramsay et al. 2013; Martín et al. 2013; Hawley et al. 2014; Davenport 2016). The occurence of WLFs on L dwarfs and young brown dwarfs (Gizis et al. 2013; Schmidt et al. 2016; Gizis et al. 2017b,a) is a proof that WLFs are common in some UCDs. In the present paper, we continue our monitoring of various UCDs using *Kepler K2* (Howell et al. 2014) data, with a goal of studying the WLF rates of various UCDs. Our targets, which include mainly late-M dwarfs and early L dwarfs, were monitored by *Kepler K2* mission during Campaigns 3, 4, 5, 6 and 12. Some targets in our sample have spectral type M6. We consider the objects with spectral types ≥M6 as UCDs in this paper. The results of work presented here is an important step that in future works will be helpful to understand different flare properties (e.g. flare energy, duration, rate, etc) in UCDs and how these properties depend on spectral type, age, mass, etc. In cases where rotation periods and ages of targets are known,

our study may shed light on the rotation-age-activity relationships in UCDs. We also include in this paper our own analysis of TRAPPIST-1 flares which were previously discussed by Vida et al. (2017) and Davenport (2017).

In this paper, we discuss flare properties in the context of the flare frequency distribution (FFD). For each star, the FFD is assumed to be fitted (over a range of energies) by a power law (Gershberg 1972; Lacy et al. 1976):

$$log\tilde{\nu} = \alpha_o - \beta logE \qquad (1)$$

where $\tilde{\nu}$ is cumulative (or integrated) flare frequency, i.e. the number of flares with energies of $\geq E$ which were detected per unit observation time. The constant α_o represents intercept at zero energy, and the constant β represents slope of the FFD. In stars which are found to have spectral index $\beta > 1$, the weakest flares contribute most to the total energy emitted by flares. In the stars with $\beta < 1$, the strongest flares contribute most to the total energy emitted by flares. Here, the phrase "total energy emitted by flares" refers to energy of all flares which were detected during a given observation time. The FFD can also be expressed in terms of differential form as:

$$dN \propto E^{-\alpha}dE \qquad (2)$$

where dN is the number of flares having energies in the range E and $E+dE$. The indices in Eq. 1 and Eq. 2 are related as $\alpha = \beta + 1$. Many studies have been done to compute the FFD in the Sun and in early-M and mid-M dwarfs. Kurochka (1987) reported the value of spectral index β to be ~ 0.80 for the energy distribution of 15000 solar flares observed during 1978-79. Hilton (2011) calculated $\beta = 0.73\pm0.1$ in the U-band energy range $10^{27.94} \leq E_U \leq 10^{30.60}$ erg for four M6-M8 dwarfs. Likewise, using a simple linear fit (Gizis et al. 2017a) reported $\beta = 0.59 \pm0.09$ in energy range 10^{31} erg to 2×10^{32} erg for a field L1 dwarf WISEP J190648.47+401106.8 (hereafter W1906+40) and $\beta = 0.66\pm0.04$ in energy range 4×10^{31} erg to 1.1×10^{33} for a 24 Myr brown dwarf 2MASS J03350208+2342356 (hereafter 2M0335+2342). Gizis et al. (2017a) used a maximum likelihood estimation (MLE) to obtain $\alpha = 1.6 \pm0.2$ and 1.8 ± 0.2 for W1906+40 and 2M0335+2342 respectively. Assuming that all the flares with energy in the range from E_{min}-E_{max} follow a FFD with a uniform power law, the total energy of all flares during observation time T can be computed by using the spectral index β. This total energy is expressed as (Gershberg & Shakhovskaia 1983):

$$\varepsilon = T \times 10^\alpha \beta(E_{max}^{1-\beta} - E_{min}^{1-\beta})/(1 - \beta) \qquad (3)$$

In this paper, we report in Section 2 on *Kepler* photometry of our 10 UCD targets, and we use the photometric data to estimate the energies of each flare. In Section 3, we discuss artificial flare injection and recovery. In Section 4, we present estimates of flare rates. In Section 5, we concentrate on the detailed properties of two superflares in our sample. Discussion of our results is presented in Section 6.

2. DATA REDUCTION AND ANALYSIS
2.1. *Targets*

There are 10 UCDs in our sample. In Table 1 we list, for each target the full name, the *Kepler* ID (EPIC), the *Kepler* magnitude, the 2MASS J magnitude, the *K2* campaign number in which the target was observed, the tangential velocity, the optical spectral type, and the distance to the star. To calculate the tangential velocity for each target, we used the relation $V_{tan} = 4.74d\mu$, where d (in parsecs) is the distance of each target as given in Table 1 and μ is the proper motion. For all but one star, we used proper motions from Gagné et al. (2015): the exception is 2M0326+1919, for which we used Schneider et al. (2016). Our sample contains two M6, three M7, three M8 and two L0 dwarfs. Most of the targets are old low mass stars and some may be brown dwarfs. The distances of two targets 2M2228-1325 and TRAPPIST-1 are taken from the literature. For the remaining stars, distances are estimated using either the M_J/ST (ST = spectral type) relationship from Dupuy & Liu (2012) or i-z/M_i relationship from Schmidt et al. 2018 (in prep). The i-z/M_i relation from Schmidt et al. (2018, in prep) is an updated version of Schmidt et al. (2010). It is based on a linear fit to the color magnitude diagram of 64 M5-L8 dwarfs and has typical uncertainties of $\sim12\%$. The ninth column in Table 1 gives the references we used to identify spectral types of each target. The tenth column indicates whether the distances were obtained from the literature or were estimated using photometry: the reader is referred to the Notes to the Table for explanations of "mjst" and "miiz" in Column 10.

2.2. *K2 photometry*

All the 10 targets listed in Table 1 were observed by *Kepler K2* in various campaigns (see the campaign number in Table 1) in both long cadence mode (~30 minute, Jenkins et al. (2010)) and short cadence mode

Table 1. Target Properties

Name	EPIC	$\tilde{K}_p$	J	Cam. #	V_{tan} (kms^{-1})[a]	Spt.	distance (pc)	Ref.	Remarks
2MASS J22285440-1325178	206050032	14.66	10.77	3	59	M6.5	11.26 ± 0.62	1	*
(LHS 523, GJ 4281, LP 760-3)									
2MASS J22021125-1109461	206135809	16.72	12.36	3	25	M6.5	22.57 ±4.16	2	mjst
2MASS J08352366+1029318	211332457	17.55	13.14	5	23	M7	32.26 ± 5.95	3	mjst
2MASS J22145070-1319590	206053352	17.74	13.46	3	55	M7.5	33.93 ± 6.26	4	mjst
2MASS J13322442-0441126	212826600	16.93	12.37	6	5.0	M7.5	20.54 ± 3.79	2	mjst
2MASS J23062928-0502285	200164267	15.91	11.40	12	61	M8	12.10 ± 0.40	5	**
(TRAPPIST-1)									
2MASS J12215066-0843197	228754562	17.93	13.52	10	29	M8	32.11 ± 5.93	4	mjst
2MASS J03264453+1919309	210764183	18.08	13.12	4	61	M8.5	24.68 ± 4.55	6	mjst
2MASS J12212770+0257198	201658777	18.40	13.17	10	14	L0	19.66 ± 2.67	6	miiz
2MASS J12321827-0951502	228730045	18.85	13.73	10	28	L0	26.41 ± 4.87	6	mjst

References: (1) Giampapa & Liebert (1986); (2) Cruz et al. (2003); (3) Burgasser et al. (2002); (4) Faherty et al. (2009); (5) Gillon et al. (2016); (6) Reid et al. (2008)

Note: mjst = "Distance estimated using a combination of 2MASS J and spectral type based on the M_J/ST relationship from Dupuy & Liu (2012)."

miiz = "Distance estimated using a combination $i - z$ color based on the $i - z/M_i$ relationship from Schmidt et al. (2018, in prep.)."

*Distance taken from Henry et al. (2004)

**Distance taken from Gillon et al. (2016)

[a] V_{tan} was calculated using the relation $V_{tan} = 4.74d\mu$

($\sim$1 minute, Gilliland et al. (2010)). We used short cadence data to study WLFs on all of our targets. We used a method similar to that described in Gizis et al. (2017b,a) to measure the photometry of our targets. In order to estimate *Kepler* magnitude which represents brightness of our targets better than the original *Kepler* magnitude K_p provided in the *Kepler* Input Catalog (KIC), we used the relation $\tilde{K}_p \equiv 25.3 - 2.5\log(\text{flux})$ (Lund et al. 2015). Here, flux is the count rate measured through a 3-pixel radius aperture. $\tilde{K}_p \approx K_p$ for most brighter (e.g., AFGK-type) stars (Gizis et al. 2017b).

Our experience in previous works (Gizis et al. 2017b,a) show that the standard light curves based on default apertures do not give the best results for the ultracool targets. So we used the target pixel files (TPFs) of each targets available in Mikulski Archive for Space Telescopes (MAST) archive instead of using the standard light curves. We began by estimating the best position of each target in each image frame. We inspected some frames by eye to estimate a threshold value of counts for the target pixels in each frame, and used the astropy-affiliated package "photutils.daofind" to estimate the centroid position in each frame. We used the median of centroids obtained for all the frames as the best position of our targets in their TPFs. We corrected the offset of centroid position in each frame due to spacecraft motion by using the information recorded as POS_CORR1 and POS_CORR2 in each TPFs. After this, we used another astropy-affiliated photometry package "photutils.aperture_photometry" to measure the photometry of each target using 2 pixel radius aperture. The same number of pixels were used by Gizis et al. (2017b,a) to measure photometry of **UCDs**. We used only good quality (Quality=0) data points. The median count rate through both the 2-pixel radius aperture (CR2) and the 3-pixel radius aperture (CR3) for each target is given in Table 2. CR2 is used for flare analysis of all targets in this paper and CR3 is only used for estimation of $\tilde{K}_p$.

2.3. *Flare detection*

Flare detection in the light curve of targets was a multi-step process. The initial step was to remove any periodic features in the light curve, which might be due to systematic or astrophysical variability. These features add complexity to the light curve, and alter the morphol-

Table 2. Median flux of targets

Name	Median flux (cnts/s) r = 2	Median flux (cnts/s) r = 3
2M2228-1325	16463	18063
2M2202-1109	2561	2695
2M0835+1029	891	1254
2M2214-1319	966	1058
2M1332-0441	1956	2220
TRAPPIST-1	5515	5717
2M1221-0843	809	884
2M0326+1919	761	771
2M1221+0257	508	577
2M1232-0951	358	381

ogy and duration of flares. We began by smoothing the original light curve of each target by using the Python package "pandas.rolling_median" (McKinney 2010) to remove the long term trends mainly caused by systematic errors in the light curve (Davenport 2016). We used a window of $w = 3$ d data points (Handberg & Lund 2014). We fitted this smoothed light curve with a third-order polynomial (as suggested by Davenport (2016)) and subtracted from original light curve. We then followed similar method described in Osten et al. (2012) to identify the flares in the smoothed light curve. We calculated relative flux $F_{rel,i}$ for each data point in the smoothed light curve, defined as:

$$F_{rel,i} = \frac{F_i - F_{mean}}{F_{mean}} \qquad (4)$$

where F_i is the flux in ith epoch and F_{mean} is the mean flux of the entire light curve of each target. This relative flux was used to identify the flare candidates. We used Lomb-Scargle periodogram to examine any other periodic features which we expect to be mainly due to astrophysical variability, e.g., due to presence of starspots. If any periodic feature was detected, we fitted the smoothed light curve with a sinusoidal function using the dominant period, and subtracted from the smoothed light curve. In this way, we prepared the detrended light curve for our targets. We then calculated a statistic ϕ_{ij} for each consecutive observation epoch (i,j) as:

$$\phi_{ij} = \left(\frac{F_{rel,i}}{\sigma_i}\right) \times \left(\frac{F_{rel,j}}{\sigma_j}\right), j = i + 1 \qquad (5)$$

Here σ_i is the error in the flux which is associated with ith epoch. This statistic defined in Welch & Stetson (1993) and Stetson (1996) was used to study variable stars using automated searches. It was later used by Kowalski et al. (2009) and Osten et al. (2012) for flare search in different stars. In order to identify the possible flare candidates in the light curve, we used the false discovery rate (FDR) analysis described in Miller et al. (2001) . This method uses a critical threshold value of the ϕ_{ij} statistic which is different for each target. To calculate this critical value of ϕ_{ij}, we first discarded all those epoch pairs for which $\phi_{ij} > 0$ but $F_{rel,i,j} < 0$. We then divided the remaining ϕ_{ij} distribution in two distributions: the null distribution for which $\phi_{ij} < 0$ and possible flare candidate distribution for which $\phi_{ij} > 0$. The absolute value of the null distribution was fitted by a Gaussian function. The parameters of this Gaussian function was then used to calculate the p-values of each ϕ_{ij} in flare candidate distribution. We then followed each step described in Appendix B of Miller et al. (2001) to calculate the critical p-value and hence the critical ϕ_{ij}. Epochs with ϕ_{ij} greater than this value of the critical ϕ_{ij} were considered to be better flare candidates in the light curve. The value of variable α which is used in Miller et al. (2001) FDR analysis is chosen to be 0.05 for *Kepler* data (based on private communication from R. Osten). This value of α signifies that no more than 5% of the epochs with ϕ_{ij} greater than the critical ϕ_{ij} are false positives (mostly due to noise in the data). We also used additional criteria, namely, that the detrended flux should exceed the photospheric level by 2.5σ. This decreased the number of flare candidates in our data set to a few hundred. The final flares were chosen by inspecting the data by eye. In this way, even for the weakest flares we ensured that there is at least a pair of epochs for which $F_{rel,i,j} > 0$: by this means, we were able to exclude any flares which had only a single measurement of flux brightening. For strong flares, there are multiple consecutive epochs with $F_{rel,i} > 0$. More detailed explanation regarding this method of flare detection can be found in Osten et al. (2012).

2.4. *Calibration of Equivalent Duration and Calculation of Flare Energy*

To calculate the flare energies, we first estimated equivalent duration (hereafter ED) of each flare. It depends on the filter used but is independent of the distance to the flaring object and so it is widely used for determining flare energies. ED of a flare is expressed as:

$$ED = \int [(F_f - F_c)/F_c]dt \qquad (6)$$

where F_f is the flare flux and F_c is the continuum flux (i.e when the star is in its quiescent state). It has units of time and gives the area under the flare light curve. It is the equivalent time during which the star (in its quiescent state) would have emitted the same amount of energy as the flare actually emitted (Gershberg 1972). We follow the method described in Gizis et al. (2017a,b) to calibrate ED in terms of energy. *Kepler* measures photometry in the wavelength range 430nm to 900nm. In case of UCDs which have lower effective temperatures, a significant part of the flux is contributed by the longer wavelength part of this range but the WLF radiation contributes flux throughout the whole range of wavelengths in the *Kepler* band. This means that a given number of WLF counts measured in the *Kepler* band will have higher mean energy than the same number of photospheric counts from the UCD (Gizis et al. 2013). For each target, we estimate the photospheric spectrum by using the matching late-M or L dwarf template spectrum (Bochanski et al. 2007; Schmidt et al. 2014) normalized to match the Pan-STARRS *i*-band photometry (Tonry et al. 2012; Chambers et al. 2016; Magnier et al. 2016) [1]. We compute the photospheric specific flux of a 10,000 K blackbody which is normalized to have the same count rate through the *Kepler* filter as the photosphere of each target. (Using an 8,000 K blackbody gives values only 2% lower: this reduction is much less than other sources of uncertainty.) We multiply this photospheric specific flux by the full width half maximum (FWHM) of the *Kepler* band pass (4000Å), $4\pi d^2$ (d = distance of target), and the *Kepler* equivalent duration to obtain *Kepler* flare energy E_{Kp}. Since a 10,000 K blackbody is more energetic for same count rate, we applied a correction factor of 1.3 to get the final estimate of E_{Kp}. The photospheric specific flux of a 10,000 K blackbody corresponding to each target is given in Table 5. Figure 1 shows the optical and near-infrared spectral energy distribution of TRAPPIST-1 and a 10,000 K flare with the same count rate through the *Kepler* filter[2]. Computation of total flare energies integrated over the ultraviolet, visible and infrared is useful to compare the results with those obtained by using other surverys.

---

[1] For LHS 523, which is too bright for Pan-STARRS, we normalize to the DENIS *I*-band photometry (Epchtein et al. 1997)

[2] For TRAPPIST-1 we used an average distance of 12.3 pc which is the average of distances mentioned in Gillon et al. (2016) and Weinberger et al. (2016)

Table 3. Flare Properties

EPIC	Peak Flare Time	ED	$\log E_{Kp}$
	(BJD - 2454833)	s	erg
206050032	2145.4316	1.1e+00	29.5
206050032	2145.5278	6.3e-01	29.3
206050032	2146.7530	2.4e+02	31.9
206050032	2147.2441	3.1e+01	31.0
206050032	2147.7570	1.5e+00	29.7

Only a portion of this table is presented here to show its form and content. A machine-readable version of the full table is available.
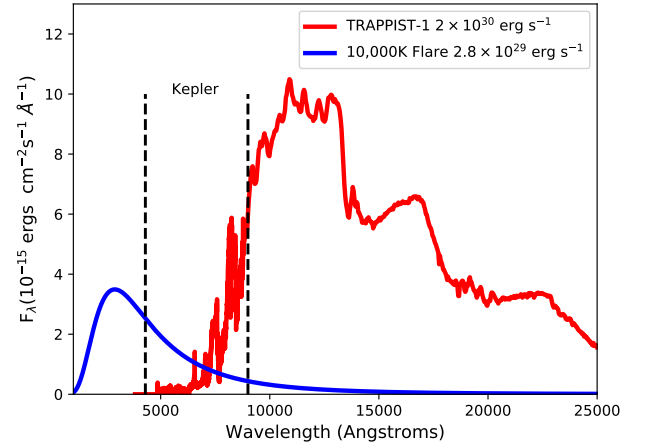

Figure 1. The optical and near-infrared spectral energy distribution of TRAPPIST-1 (red) and a hypothetical 10,000 K blackbody (blue). The wavelength range in between vertical dashed lines is *Kepler* band. Using the distance of 12.3 pc, the bolometric luminosity of TRAPPIST-1 is 2.0×10^{30} erg s^{-1} and that of 10,000 K flare is 2.8×10^{29} erg s^{-1}.

For the 10,000 K blackbody flare model we adopt, this bolometric energy (UV/optical/infrared) is 3.1 times the E_{Kp} we report. Likewise, for an 8,000 K blackbody the factor is 2.5. Gizis et al. (2013) argued this range is similar to that seen in an M dwarf flare by Hawley & Pettersen (1991). In Table 3, we list the time at which peak flare emission occured, the equivalent duration, and the *Kepler* energy for all of the flares which we identified in our targets.

3. ARTIFICIAL FLARE INJECTION AND ESTIMATION OF LOWEST DETECTABLE FLARE ENERGY

In order to get an estimate of the minimum flare energy which could be detected by our algorithm, we

generated artificial flares of randomly chosen amplitude and duration using Davenport model (Davenport et al. 2014). This was done by a slight modification of a similar module used in software package known as "appaloosa" (Davenport et al. 2016). Then we injected the artificial flares at random times to the detrended light curve with 1-σ noise. To prepare this detrended light curve, we followed similar detrending process described in Section 2 and masked all other fluxes greater than 1-σ level from the median flux. For simplicity, all injected artificial flares were single-peak "classic flares". Care was taken to avoid any overlapping of the injected flares. We injected 10 artificial flares at once and used our algorithm to detect them. We kept track of times at which the artificial flares were injected and their equivalent durations. We repeated this process 1,000 times, so a total of 10,000 artificial flares were generated: however, due to our restriction to non-overlapping events, some fraction of the 10,000 couldn't be injected. We then calculated the flare energies of the injected artificial flares and compared these values with the energies we recovered by means of our algorithm. We found that weak flares having energies less than a certain energy were not detected by our algorithm. The light curves of different targets have different noise levels, so the minimum detectable energy of weak flares as found by our algorithm is different for each target. To estimate this minimum energy, we repeated the above process separately for each target. A list of minimum energies of artificial flares injected and later detected by our algorithm is given in Table 4. For flare analysis, we discarded all the flares (if any) having energies less than the minimum energy of the artificial flares detected by our algorithm.

4. FLARE STATISTICS AND FLARE ENERGY SPECTRUM OF TARGET UCDS

Table 5 lists various properties of flares on sample targets. In this table, 'specific flux' is the flux per cm^2 per second per Angstrom for a 10,000 K blackbody which has the same number of counts as the target in *Kepler* bandpass. The column 'Periodic Features' gives information if any periodic feature is seen in the light curve of each target after removing the long term trends using rolling median method. If any periodicity is seen, the dominant period is listed. The periodicity might be due to the presence of starspots, and most probably gives an indication of the rotation period of the target. N is the number of flares observed on a given target during the entire interval T of *K2* observations of that target (for T values, see Table 6). Likewise, $E_{Kp,min}$ is

Table 4. Minimum energies of injected and detected artificial flares

Name	E_{Kp}, min (10^{30} erg) injected	E_{Kp}, min (10^{30} erg) detected
2M2228-1325	0.014	0.18
2M2202-1109	0.008	0.65
2M0835+1029	0.006	0.93
2M2214-1319	0.004	1.3
2M1332-0441	0.009	0.59
TRAPPIST-1	0.004	0.17
2M1221-0843	0.002	1.3
2M0326+1919	0.021	0.62
2M1221+0257	0.006	0.37
2M1232-0951	0.004	0.83

the minimum *Kepler* energy of all the identified flares on a given target and $E_{Kp,max}$ is the maximum *Kepler* energy of all the identified flares on a given target.

Table 6 lists the values of fitted parameters for the FFD of each of our targets. In this table T is the total observation time for a given target, β and α_o are the fitted values of parameters in Eq. 1. Likewise, E_{min} and E_{max} are the minimum and maximum *Kepler* energies used for fitting. The total observation time T (in seconds) is computed by counting the total number of good (Quality = 0) data points and multiplying by 58.85 s which is the correct exposure time equivalent to 1 short cadence. We used the maximum-likelihood method described in Hogg et al. (2010) and implemented in the routine known as "emcee" (Foreman-Mackey et al. 2013) to fit a straight line to our data (in log scale) and hence obtain the optimal values of parameters β and α_o. Here we report the intercept α_o corresponding to energy 10^{30} erg, not the zero energy. It will be helpful in comparing the flare rates of our targets with previously reported flare rates of other targets observed by *Kepler and K2*, most of which have flare energies greater than 10^{30} erg (Ramsay et al. 2013; Hawley et al. 2014; Davenport 2016; Gizis et al. 2017a). The routine "emcee" uses the standard Metropolis-Hastings Markov-Chain Monte Carlo (MCMC) procedure for marginalization and uncertainty estimation. We neglected the highest observed energy for fitting the line to reduce any bias in the analysis. Since 2M2228-1325 has a heavy-tailed distribution, we need to select a minimum value of energy to be considered for fitting. This minimum value was chosen on the basis of fitting for broken power law
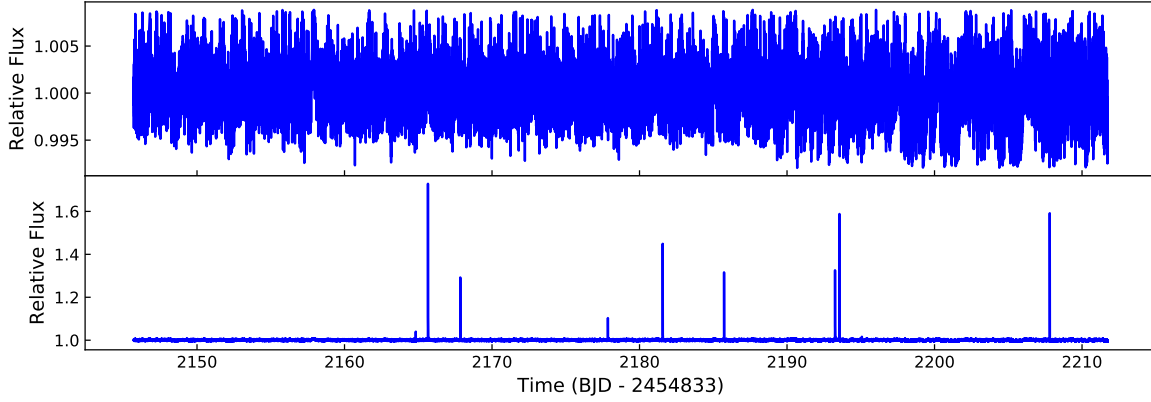
Figure 2. An example of artificial flare injection in 2M2228-1325 light curve. The upper plot is detrended light curve with 1-σ noise and the lower plot is the light curve with artificial flares injected at random times.

Table 5. Flare statistics

Target	Sp. flux (erg cm^{-2} s^{-1} $\mathring{A}^{-1}$)	Periodic feature	N	E_{Kp}, min (10^{30} erg)	E_{Kp}, max (10^{30} erg)
2M2228-1325	3.66×10^{-15}	No	50	0.19	72
2M2202-1109	4.64×10^{-16}	Yes (0.42 d)	50	0.64	310
2M0835+1029	1.55×10^{-16}	No	11	1.1	2900
2M2214-1319	1.64×10^{-16}	No	26	2.2	350
2M1332-0441	3.62×10^{-16}	No	31	0.69	85
TRAPPIST-1	8.95×10^{-16}	Yes (3.3 d)	39	0.21	230
2M1221-0843	1.47×10^{-16}	Yes (0.27 d)	36	1.4	150
2M0326+1919	1.40×10^{-16}	Yes (0.97 d)	18	0.67	55
2M1221+0257	1.10×10^{-16}	Yes (0.18 d)	11	0.48	25
2M1232-0951	6.29×10^{-17}	No	11	0.82	1200

discussed below. For targets which do not have a heavy tailed distribution, all flares, even those with the lowest energies, were considered for fitting. We also used the analytic solution to get the estimate of parameter α which is derived in Clauset et al. (2009) and references therein. Here we denote this estimate as $\hat{\alpha}$ which is the maximum likelihood estimator (MLE) of true parameter α and is expressed as:

$$\hat{\alpha} = 1 + n \left[\sum_{i=1}^{n} ln \frac{E_i}{E_{min}} \right]^{-1} \quad (7)$$

with error

$$\sigma = \frac{\sqrt{n+1}(\hat{\alpha} - 1)}{n} \quad (8)$$

. Here n is the number of flares and E_i, i $= 1...n$ are the observed values of energies E such that $E_i \geq E_{min}$.

The MLE solution $\hat{\alpha}$ is an unbiased estimator of α in the asymptotic limit of large sample size, $n \to \infty$. In addition, a more reliable estimate for parameter α can be obtained for sample size n $\gtrsim 50$ (Clauset et al. 2009). For small sample sizes n, Arnold (2015) suggests the value of $\hat{\alpha}$ obtained by using Eq. 7 can be multiplied by a factor of $(n-2)/n$ in order to make the result unbiased. The unbiased values of $\hat{\alpha}$ for each target are listed in Table 6. The same energy range used for fitting the power law FFD is used for estimating $\hat{\alpha}$. As the number of flares on most of our targets is unfortunately rather small for a more accurate estimation of parameter α using the analytic solution: we will use the results obtained by using the "emcee" routine for discussion and comparison of our results with previous works. Table 6 also lists the slopes of FFDs for 2M0335+2342 and W1906+40, obtained by using the methods described above. It should be noted that they are slightly differ-

ent from the values reported in previous papers because somewhat different energy intervals were chosen for fitting.

Figure 3 shows the FFD of each target in the sample. The FFD for each star is presented separately in each panel, and the panels are arranged in order of increasingly late spectral type. The FFDs of other targets in the sample are also plotted in the background of each panel to enable the reader to compare the FFD of a given target with others in our sample. Figure 4 compares FFDs of all the targets in sample. It should be noted that the fitted line of 2M1221+0257 covers a very small range of energy which is less than one order in magnitude. Likewise, Figure 5 shows a comparison of the FFD for a young brown dwarf 2M0335+2342 with the FFD for an L0 dwarf 2M1232-0951.

4.1. Possibility of a broken power law or a power law with exponential cutoff in the FFD of some UCDs

The presence of long tails at high energies in the FFDs suggests that a single power law might not be the optimal fit to the FFD of all UCDs. In the case of 2 of our targets (2M2228-1325 and 2M0326+1919), we tried to fit two different models: (i) a broken power law, and (ii) a power law combined with an exponential cutoff. Results are shown in Figures 6 and 7. The broken power law model can be expressed as:

$$f(E) = \begin{cases} A(E/E_{break})^{-\alpha_1} : E < E_{break} \\ A(E/E_{break})^{-\alpha_2} : E > E_{break} \end{cases} \quad (9)$$

while the power law with exponential cutoff can be expressed as:

$$f(E) = A(E/E_0)^{-\alpha} exp(-E/E_{cutoff}) \quad (10)$$

We used the astropy-affiliated packages "modeling.powerlaws.BrokenPowerLaw1D" and "modeling.powerlaws.ExponentialCutoffPowerLaw1D" to estimate the model parameters. And we used the astropy-affilicated package "modeling.fitting.LevMarLSQFitter" to fit the data. The later package uses the Levenberg-Marquardt algorithm and least squares statistic for fitting. We used a likelihood ratio test to decide which model better fits the observed data, by considering the broken power law model as alternate, and the power law with exponential cutoff as the null model. In the case of 2M2228-1325, we found that the broken power law provides a better fit to the data with $\alpha_1 = 0.20$, $\alpha_2 = 0.83$, $E_{break} = 3.25 \times 10^{30}$ erg and $A = 29.86$. The p-value of the

likelihood-ratio test statistic is 0.005 (i.e. we reject our null model for a significance level of 0.05). We used the energies greater than E_{break} for determining the slope of the FFD. But, in the case of 2M0326+1919, we found that the power law with exponential cutoff provides a better fit to the data. In this case, the fitted parameters are $A = 15.15$, $E_{cutoff} = 3.83 \times 10^{31}$ erg, $E_0 = 1.40 \times 10^{30}$ erg and $\alpha = 0.23$. The p-value of the test statistic is 0.60 (i.e. we accept our null model for a significance level of 0.05). The possible break in the power law could be due to a number of factors, including the sensitivity of the instrument in observing weak flares, or saturation, or an upper limit on the energy which any flare on a given target is able to release (Gershberg 2005). As far as we have been able to determine, broken power law FFD's laws are seldom discussed in literature.

5. SUPERFLARES OBSERVED ON TWO UCDS

One of the advantages of short cadence *Kepler* data is that it helps to study the time scales associated with rapid rise, rapid decay and gradual decay phase of superflares (flares with energies $\geq 10^{33}$ erg). Here we present the photometry of two superflares observed on our targets.

5.1. Photometry of superflare observed on L0 dwarf 2MASS J12321827-0951502

We observed a superflare on L0 dwarf 2M1232-0951 at *Kepler* time 2811.7662319, when the flare flux rose to 51529 cnts/s ($\tilde{K}_p = 13.44$, $\Delta \tilde{K}_p = -5.41$): this count rate is ∼144 times larger than the photospheric level (358 cnts/s). To determine the relevant time-scales of the flare, we used Davenport et al. (2014) (hereafter D14) model to fit the flare light curve. This yields values for the time scale $t_{1/2}$ associated with the rise of flux from and return to half maximum flux. The model also yields values for two decay time scales, one rapid (close to flare maximum), and the other gradual (later in the flare). The D14 model uses a flare template that was based on the flare properties of M4 dwarf GJ 1243 using *Kepler* short cadence data. In this model, the rapid rise phase is best fitted by using a fourth order polynomial, and the decay phase is best fitted by using sum of two exponentials which can be expressed as:

$$\Delta F = A(\alpha_i e^{-\gamma_i \Delta t/t_{1/2}} + \alpha_g e^{-\gamma_g \Delta t/t_{1/2}}) \quad (11)$$

where ΔF is flare only flux, A is flare amplitude and $\Delta t = t - t_f$ (t_f is the peak flare time). In D14 template, the values of the different parameters of Eq.(11) are $\alpha_i = 0.6890(\pm 0.0008)$, $\alpha_g = 0.3030(\pm 0.0009)$, $\gamma_i = 1.600(\pm 0.003)$ and $\gamma_g = 0.2783(\pm 0.0007)$. Schmidt et al. (2016) used this model to estimate the value of $t_{1/2}$ to

Table 6. Power law fits to FFDs of targets

Name	T	β	$\alpha=\beta+1$	α_o	$\hat{\alpha}$	E_{min}	E_{max}
	(days)					$(10^{30}$ erg)	$(10^{30}$ erg)
2M2228-1325	66.8	1.03±0.05	2.03	-1.14±0.05	1.90±0.18	3.6	32
2M2202-1109	67.5	0.65±0.02	1.65	-1.50±0.02	1.49±0.07	0.64	100
2M0835+1029	73.3	0.65±0.05	1.65	-2.11±0.03	1.43±0.14	1.1	15
2M2214-1319	66.9	0.70 ±0.02	1.70	-1.45±0.02	1.54±0.11	2.2	160
2M1332-0441	76.4	0.57±0.03	1.57	-1.81±0.02	1.49±0.09	0.69	38
TRAPPIST-1	70.6	0.61±0.02	1.61	-1.94 ±0.01	1.47±0.08	0.21	18
2M1221-0843	53.4	0.75 ±0.02	1.75	-1.37±0.02	1.66±0.12	1.4	49
2M0326+1919	69.2	0.45 ±0.04	1.45	-1.98± 0.03	1.32±0.08	0.67	44
2M1221+0257	53.5	1.04±0.08	2.04	-2.34±0.02	1.85 ±0.28	0.48	2.3
2M1232-0951	53.5	0.34±0.04	1.34	-2.16 ±0.03	1.37 ±0.12	0.82	130
2M0335+2342	69.0	0.64 ±0.03	1.64	-1.23 ±0.05	1.77±0.19	15	320
W1906+40	83.0	0.52 ±0.05	1.52	-2.12 ±0.03	1.37 ±0.09	0.56	19

Note: The intercept α_o reported in this table gives the flare rate for flare energy 10^{30} erg, not the zero energy. See the text for more description.
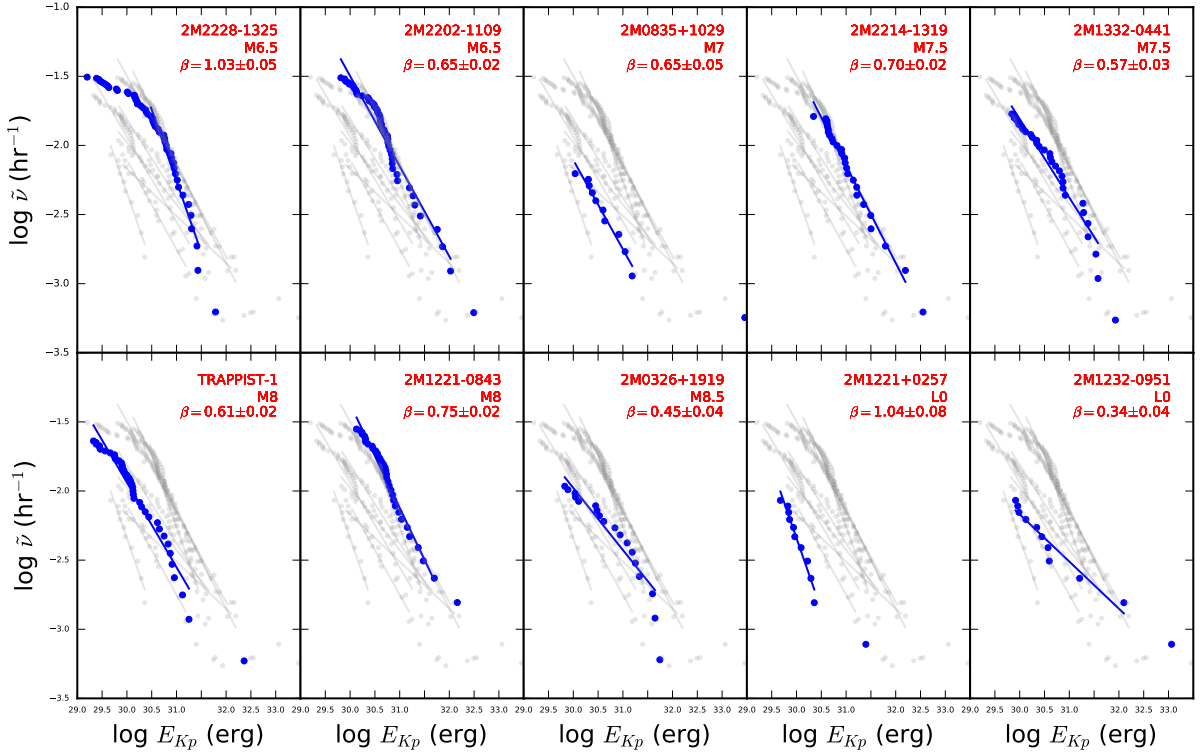
Figure 3. Individual FFD of all UCDs discussed in this paper. The FFDs are presented according the spectral order of targets. The blue dots represent the observed data and the blue solid line represents the fitted model in each plot. The FFDs of all remaining targets are also plotted in the background to make easy for comparison.
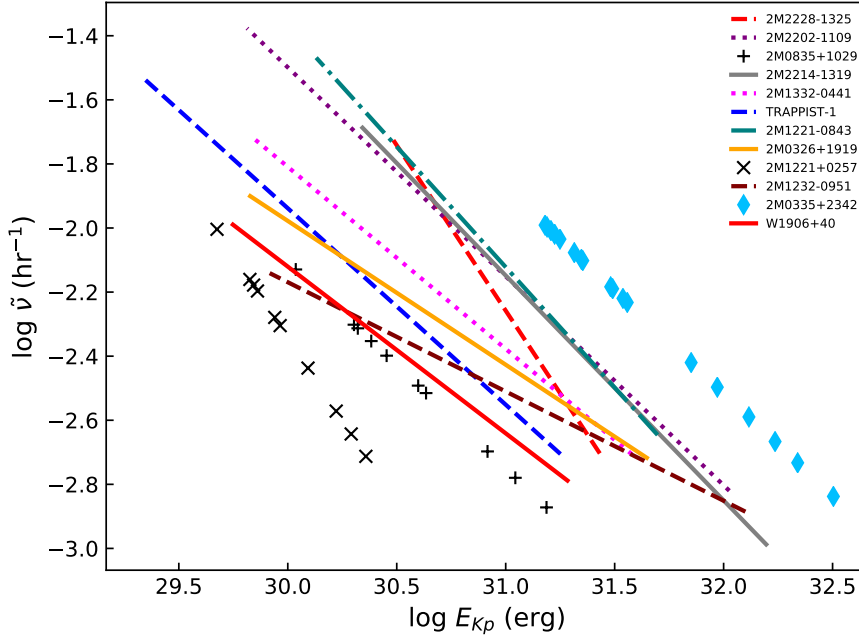
Figure 4. Comparison of fitted FFDs of all UCDs in our sample. The maximum observed energy was not included to minimize biasness. The energy range used for fitting is given in Table 6. FFDs of two more UCDs: W1906+40 and 2M0335+2342 are also included here. We used the method described in this paper to fit their FFDs.
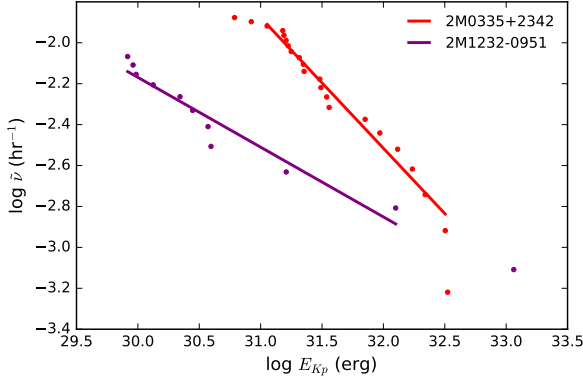
Figure 5. Comparison of FFD of a young brown dwarf 2M0335+2342 (red) and L0 dwarf 2M1232-0951 (purple). The dots represent observed data and solid lines represent the fitted power law model. This plot suggests that 2M1232-0951 has flare rate comparable to a 24 Myr young brown dwarf in case of high energy flares despite having cool atmosphere.
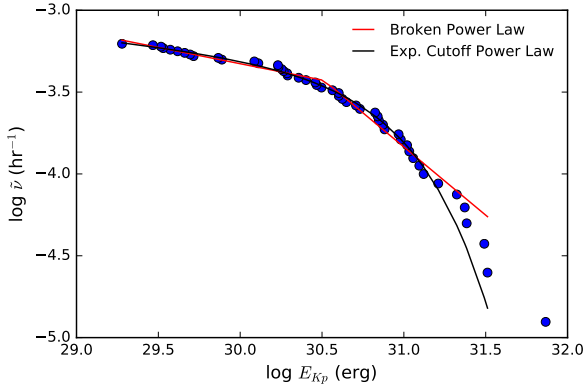
Figure 6. Comparison between broken power law and power law with cutoff in case of 2M2228-1325.
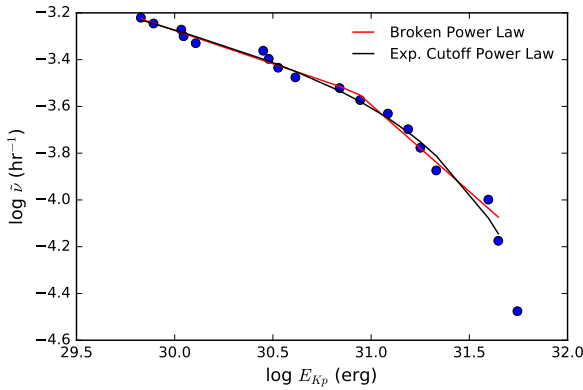
Figure 7. Comparison between broken power law and power law with cutoff in case of 2M0326+1919.

be in the range 3 (best fit) to 6.2 (minimal fit) minutes for a superflare observed on L0 dwarf ASASSN-16ae. Likewise, Gizis et al. (2017b) estimated $t_{1/2} = 6.9$ minutes for L1 dwarf W1906+40 using same model. Slightly different value of parameters were used by Gizis et al. (2017b) to fit a superflare on the L1 dwarf SDSSp J005406.55-003101.8 to estimate $t_{1/2} = 7.8$ minutes. Here, the estimation of $t_{1/2}$ for 2M1232-0951 is done using *Kepler* short cadence data, so it is more accurate than those reported for ASASSN-16ae and SDSSp J005406.55-003101.8. To fit the flare of interest to us here (i.e. the superflare on 2M1232-0951), we started by examining if the D14 model could fit the observed data. However, we found that it did not provide an especially good fit for the late decay phase. To get an initial estimation of decay phase time scale, we fitted the late decay phase separately by a single exponential curve and used the parameters obtained in this way to fit the entire curve. Figure 8 shows the observed flux and fitted model[3]. At first glance in Figure 8(a), there seems to be a good agreement between observed data and fitted model. But, the discrepancy can be clearly seen in log-log version of same plot as shown in Figure 8(b). The values of fitted parameters for this flare are: $\alpha_i = 0.9691$, $\alpha_g = 0.0310$, $\gamma_i = 0.4551$ and $\gamma_g = 0.01543$. Likewise other fitted parameters are $A = 51005.76$, $t_{1/2} = 1.054$ minute and time of flare = 2811.7661 days. The observation shows that the flux decreases from its maximum value 51529 cnts/s to about one-half of its maximum value which is 27370 cnts/s in an interval of about 1 minute. Since the best cadence time for gathering *K2* data is also about 1 minute, we estimate that a more accurate value of $t_{1/2}$ could be around 2 minutes for this superflare. The ED of this flare is 11.4 hours and its total bolometric (UV/optical/infrared) energy is 3.6×10^{33} erg. The total flare duration is 4.2 hours.

Using the above fitted parameters and solving for the value of $\Delta t = t\text{-}t_f$ at which impulsive decay switches to gradual decay, we get $\Delta t = 7.83 t_{1/2}$ after the peak flare which occurs at $\Delta t = 0$. Now using this time reference, we found that the rise phase contains 22.15%, the impulsive decay phase 38.70% and the gradual decay phase 39.15% of the total energy.

---

[3] This curve is based on medians of parameters of at least 1.5 million samples generated by using Markov Chain Monte Carlo sampling of the posterior function using emcee (Foreman-Mackey et al. (2013) with uniform priors). All the flare fits presented in this paper are fitted using this method. For better results, we ensured that the mean acceptance fraction of the sample ensemble to be between 0.25 and 0.5 as mentioned in emcee documentation.
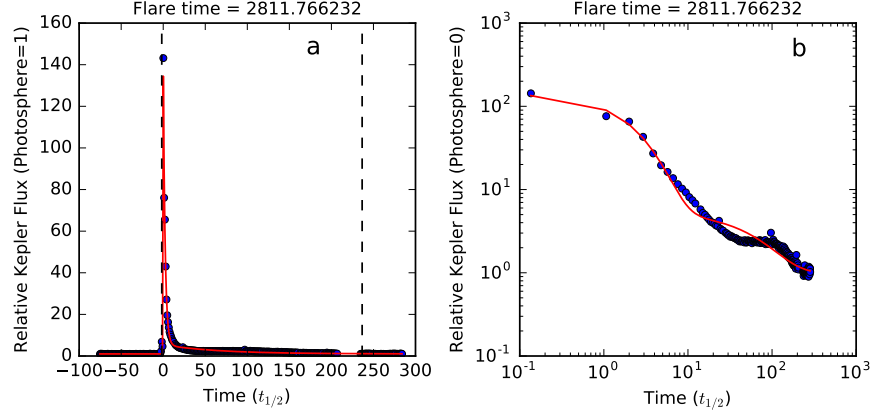
Figure 8. (a) Superflare observed on 2M1232-0951. The blue dots represent the observed flux and the red curve represents the fitted flux using slightly different parameters in D14 model. The time is zero centered at peak flare time and scaled by $t_{1/2}$. The vertical dashed lines represent the flare start and end times. (b) This plot is log-log version of plot shown in (a).

5.2. Photometry of superflare observed on M7 dwarf 2MASS J08352366+1029318

We also observed a superflare on M7 dwarf 2M0835+1029 at *Kepler* time 2379.88288303, when the flare flux is 53213 cnts/s ($\tilde{K}_p$ = 13.26, $\Delta\tilde{K}_p$ = -4.29): this peak flux is $\sim$60 times larger than the photospheric level (891 cnts/s). For this flare also, we found the original parameters of D14 model do not fit the data particularly well. We consider that we need to make slight changes to the D14 values. We used a fitting procedure similar to that used for the 2M1232-0951 superflare discussed in Section 5.1. We found the following values for the fitted parameters of the M7 superflare: α_i = 0.8182, α_g = 0.1818, γ_i = 0.6204 and γ_g = 0.08467. Likewise, we found the other fitted parameters are A= 58480, $t_{1/2}$ = 1.73 minutes and time of flare = 2379.8825 days. Both the observed flux and fitted model for this superflare are shown in Figure 9(a). This figure and its corresponding log-log version Figure 9(b) show that there is better agreement between the observed flare curve and fitted model than in case of the superflare observed on the L0 dwarf 2M1232-0951. The ED of this flare is 7.7 hours and its total bolometric energy (UV/optical/infrared) is 8.9×10^{33} erg. The total flare duration is 4.5 hours. In this superflare, we found that that the value of Δt = t-t_f at which transition between impulsive decay and gradual decay takes place is Δt = $2.81t_{1/2}$ after the peak flare ($\Delta t = 0$). Now using this time reference, we found that the rise phase contains 19.57%, the impulsive decay phase contains 25.86% and the gradual decay phase 54.58% of the total flare energy.

6. DISCUSSION AND CONCLUSIONS

We identified a total of 283 white light flares in our sample of 10 UCDs. The flares we detected have *Kepler*

energies in the range log $E_{Kp} \sim$(29 - 33.5) erg, and the flares follow power law distributions with slopes $-\alpha$ lying in the range -1.3 & -2.0. The values of these slopes were determined by using maximum-likelihood method of fitting a straight line, as implemented in "emcee" software. We also estimated the values of slopes using an analytical method. The presence of noise in the data makes it difficult to detect the weakest flares in UCDs. Due to this, the minimum detectable energy is $>10^{29}$ erg in our targets. The late-M dwarfs in our sample have FFD comparable to active mid and late-M dwarfs studied by Hilton (2011). Compared to Hilton (2011), the flares observed by *Kepler* have higher energy and are less frequent. Yet, we find similar slopes ($-\alpha$). The slopes of late-M dwarfs lie in between -1.5 & -1.8 except for M6.5 dwarf 2M2228-1325 for which $-\alpha$ = -2.0. We should note that the slopes also depend on the range of energy chosen for fitting. We also analyzed flares on TRAPPIST-1 using the official *K2* pipeline reduced data. We identified 39 good flares on it with bolometric (UV/optical/infrared) flare energies in the range from 6.5×10^{29} to 7.2×10^{32} erg. We find that its FFD has a slope of $-\alpha$ = -1.6. Previously, Vida et al. (2017) published the FFD of TRAPPIST-1 using raw data and estimated similar value of the slope but in a slightly different energy range 1.3×10^{30} - 1.2×10^{33} erg. In comparison to other M8 dwarfs in our sample, TRAPPIST-1 has steeper slope than M8.5 dwarf: 2M03264+1919 ($-\alpha$ = -1.5) and shallower slope than another M8 dwarf 2M1221-0843 ($-\alpha$ = -1.8) in slightly different energy ranges.

In Figure 10, we compare the average flare rates of UCDs with a range of spectral types. The average flare rates are computed by mixing both active and less
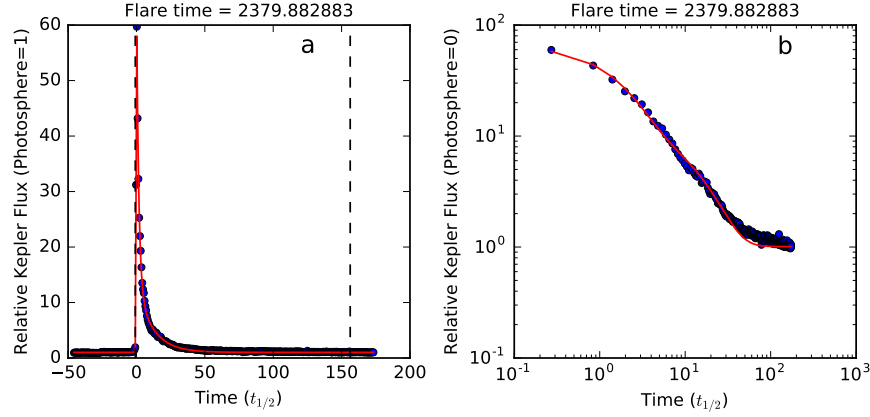
Figure 9. (a) Superflare observed on 2M0835+1029. The blue dots represent the observed flux and the red curve represents the fitted flux using slightly different parameters in D14 model. The vertical dashed lines represent the start and stop times of flare. The time is zero centered at peak flare time and scaled by $t_{1/2}$. (b) This plot is log-log version of plot shown in (a).
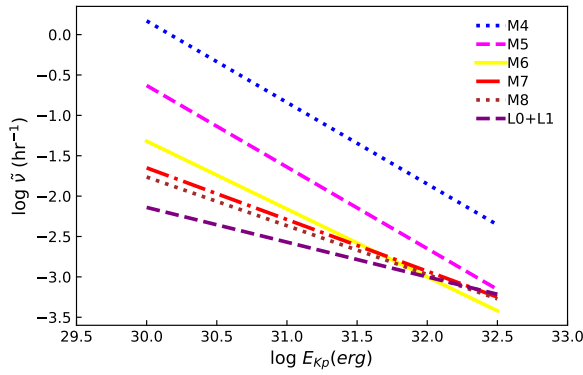

Figure 10. Comparison of average flare rates of each spectral type in our sample with flare rates of GJ1243 (M4) and GJ1245 AB (M5) taken from Hawley et al. (2014) and Lurie et al. (2015).

Figure 11. Bolometric energies of biggest flares observed on all five L dwarfs.

active targets of similar spectral types. For the L0+L1 catagory, we used average flare rate of 2M1232-0951 (L0) and W1906+40 (L1). For comparison with previous works, we compare the flare rates of M4 dwarf GJ 1243 and M5 dwarf GJ 1245 AB taken from Hawley et al. (2014) and Lurie et al. (2015) who also report the slopes of FFDs using *Kepler* energies of flares. We can see that the flare rates of GJ 1243 are higher than those of late-M dwarfs and early L dwarfs by about two orders of magnitude for flares with energy 10^{30} erg. In addition, Figure 10 shows cool stars tend to have shallower slopes. The β values of averaged FFDs in Figure 10 are 0.84, 0.64, 0.60 and 0.43 for M6, M7, M8 and L0+L1 spectral types respectively.

The L dwarfs have the lowest flare rates for small energy flares. The FFD of L0 dwarf 2M1232-0951 has a very

shallow slope ($-\alpha$ = -1.3) compared to other UCDs in sample. The fitted line covers three orders in magnitude. A shallower slope signifies that occurence rate of bigger flares is higher in this target than other targets in our sample. The FFD of another L dwarf W1906+40 as obtained by Gizis et al. (2013) also suggests that L dwarfs have shallower slopes. Figure 5 compares the FFD of 2M1232-0951 with that of young BD 2M0335+2342. The convergence of two fitted lines at observed high flare energies suggests that both targets have comparable flare rate for such energies. For flare energy log $E_{Kp} \sim 29.0$ erg, 2M1232-0951 has lower flare rate with the difference being more than one order of magnitude. The convergence of lines is also clearly seen in Figure 10 in case of spectral types $\geq$M5, which again indicates comparable flare rates for observed higher flare energies. More fascinating fact about 2M1232-0951 is that it has a flare with the second highest energy among all the targets in our sample. How does it have better efficiency

in converting magnetic energy to higher energy flares than those with low energies? We have to understand the relationship between the magnetic field, volume and rate at which the magnetic field lines are stretched to store energy. The stretching of magnetic field lines may also depend on speed of convective flows.

The steeper slope ($-\alpha$ = -2.0) which we have obtained in case of another L0 dwarf (2M1221+0257) is valid for a very narrow energy range (log E_{Kp} ~29.7 - 30.4 erg). There is one high energy flare on this target but its energy was not included for fitting purpose. It will be inappropriate to compare the flare rates of two L dwarfs based on the slopes obtained here as the energy ranges considered for obtaining the slopes are very different. As of now, white light flares are observed on five L dwarfs. Two such flaring L dwarfs are discussed in this paper. The remaining three are discussed in Gizis et al. (2013), Schmidt et al. (2016) and Gizis et al. (2017b). Figure 11 shows the bolometric (UV/optical/infrared) flare energy distribution of the biggest flares observed on all five L dwarfs. ASASSN-16ae has the largest bolometric flare energy which is > 6.2×10^{34} erg (Schmidt et al. 2016).

The fraction of L0 and L1 dwarfs having chromospheric H_α emission is ~90% and ~67%, respectively, with a decline in H_α activity in comparison to earlier spectral types (Schmidt et al. 2015). This may be due to the lower effective temperatures and hence less ionization reducing the effectiveness of the interaction between the magnetic field and gas (Mohanty et al. 2002). In addition, the L0-L1 dwarfs do not have clearly developed rotation-activity connections despite being rapid rotators (Reiners & Basri 2008). We do not have proper information about the rotation periods, or ages, or activity levels for the two L dwarfs 2M1232-0951 and 2M1221+0257. But what we know is that 2M1232-0951 has a longer time-scale variability (Koen 2013), and 2M1221+0257 has a variable H_α emission with equivalent width 25.65$\mathring{A}$ and log$L_{H\alpha}/L_{bol}$ = -4.18 (Reiners & Basri 2008). This limited information is not enough to interpret the observed results of L dwarfs. One possible physical process which might contribute to shallower FFD slopes in L dwarfs is discussed by Mullan & Paudel (2018). The model is based on production of flares by instability in coronal magnetic loops in which the footpoints of magnetic flux ropes are subject to random walk due to convective flows. Shallower slopes of the FFD are found to arise in the presence of reduced electrical conductivity in the coolest stars.

Table 7. Average slopes of FFDs of targets classified by kinematic age

Target type	Average V_{tan} km s^{-1}	Average β
old	59	0.70
young	28	0.58
very young	10	0.61

We observed superflares on two targets: 2M1232-0951 and 2M0835+1029. Those flares have total bolometric (UV/optical/infrared) energies 3.6×10^{33} erg and 8.9×10^{33} erg. They have very short FWHM time scales of ~2 minutes. In the case of 2M1232-0951, the superflare brightened by a factor of ~144 relative to the quiescent photospheric level. Likewise, the superflare observed on 2M0835+1029 brightened by a factor of ~60 relative to the quiescent photospheric level. Another superflare with bolometric (UV/optical/infrared) energy 2.6×10^{34} was observed on a 130-Myr old brown dwarf CFHT-PL-17 (Gizis et al. 2017a). We have also detected the most powerful white light flare on another young brown dwarf (Paudel et al. 2018). The presence of superflares on so many cool targets (the flares discussed here, plus the flares discussed in Schmidt et al. (2016) and Gizis et al. (2017b)) suggests that this is a universal phenomenon which is commonly observed on solar-type stars (Maehara et al. 2012; Shibayama et al. 2013; Notsu et al. 2013). It also suggests that very low mass stars and brown dwarfs are magnetically active despite having cool atmospheres. The underlying nature of magnetic dynamo is still unknown in such objects.

If we make use of the tangential velocity estimates as age indicators, we find that our targets have different ages. TRAPPIST-1 and 2M0326+1919 seem to be the oldest targets and 2M1332-0441 seems to be the youngest one. In support of our claim of a great age for TRAPPIST-1, we may cite Burgasser & Mamajek (2017) who have reported an age of 7.6±2.2 Gyr. Despite having the same tangential velocity and spectral type, the FFD of TRAPPIST-1 has a slightly steeper slope than 2M0326+1919: moreover, TRAPPIST-1 has a higher occurence rate of low energy flares than the same M8.5 dwarf. The FFD of 2M2228-1325 has a steeper slope than 2M2202-1109, though 2M2228-1325 has a larger tangential velocity and the same spectral type. Likewise, 2M1332-0441 has a shallower slope than other targets of similar spectral type, despite having the lowest tangential velocity, and is therefore presumably the youngest. In Figure 12, we compare the flare rates of
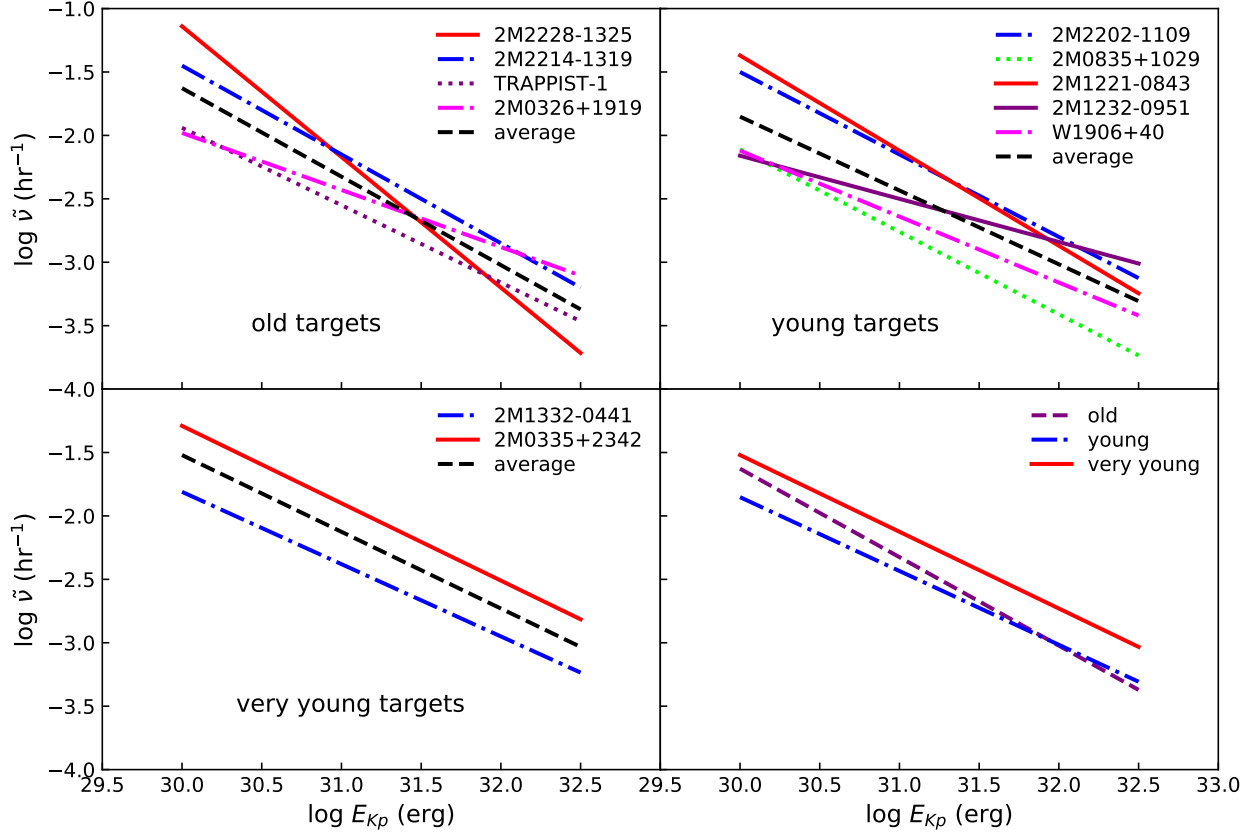
Figure 12. Comparison of flare rates of targets of different kinematic ages. We used our tangential velocity estimates as age indicators. The upper two plots compare flare rates of old and young targets. The lower left plot compares the flare rates of very young targets and the lower right plot compares the average flare rates of old, young and very young targets. The dashed lines in the upper two plots and the lower left plot show the average flare rates of targets included in those plots.

targets having similar ages with different spectral types. The targets are categorized as very young, young, or old according to the tangential velocity estimates we have. The average tangential velocities and average slopes of FFDs of the three categories of targets are listed in Table 7. 2M1221+0257 is not included for this purpose because its observed flare energies lie in a very narrow range. While there is a slight difference in the slopes of FFDs of targets of various ages in Table 7, we cannot conclude anything definitive because of the small sample sizes.

There is diversity both in age and spectral type of our targets. The diversity in the slopes of FFDs and flare rates observed in our targets suggests that the flare rate of a given target may depend on many factors rather than just age and spectral type (effective tem-

perature). Some of such factors may be rotation rate, magnetic field topology, the number of spots, etc. It will be interesting to compare the flare rates of some targets which will again be observed by *K2* in future campaigns. If we can use new data for the same targets, we may be able to confirm if the flare rates of UCDs remain constant, change slightly or change drastically within short intervals of time. Due to small sample size and smaller number of flares detected on faint targets, we cannot conclude any relation between the spectral type or age and the slope $-\alpha$ of FFD. We need to study the FFDs for a larger sample of UCDs over a wide range of energies to see if any such relations exist. The results of Lee et al. (2016) suggests that the occurence rate (R) of big solar flares and front-side halo coronal mass ejections are higher during the descending phase of solar cycle than other phases. They report a strong

anti-correlation between R and annual average latitude of sunspot groups. Is this just a coincidence or due to some underlying physical phenomenon? We may also think of same scenario in case of our targets. Route (2016) has reported some evidence of magnetic cycles in UCDs. The flare rate on UCDs might depend on the phase of their magnetic cycle. More information about rotational velocities of UCDs will be helpful to understand such correlations (if they exist).

The FFDs of two of our targets seem to show deviations from a single power law dependence. Using the likelihood ratio test, we found that the FFD of one target (2M2228-1325) seems to follow a broken power law distribution while the FFD of another target (2M0326+1919) seems to follow a power law distribution with exponential cutoff. Unfortunately, since the number of flares observed on both targets is small, we cannot conclude if such deviations of FFDs from regular power laws are due to instrumental sensitivity or due to saturation at large energies. Gershberg (2005) (p. 227) mentions that the curvatures seen in FFD of some targets were absent when they were observed again, and the number of observed flares was increased. Curved FFDs can be seen in case of EQ Peg, UV Cet and AD Leo in Figure 38 (p. 224) of Gershberg (2005). Other examples of departures of FFD from single power-laws are provided by GJ 1243 and GJ 1245 AB (Hawley et al. 2014), and by KIC 11551430 (Davenport 2016).

The flare rates of UCDs reported in this paper should be helpful in predicting the number of flares on targets of similar types, which could be observed by future photometric surveys. They are also very important for gyrochronology and studying the planets in habitable zone of stars like TRAPPIST-1. The biggest flares might be capable of damaging atmospheric chemistry and other habitable conditions of the planets. However, detailed discussion about the possible impact of flares of TRAPPIST-1 on its planetary atmospheres is beyond the scope of this paper. One can find the necessary information in recent papers like Roettenbacher & Kane (2017); Tilley et al. (2017), etc.

Facilities: Kepler

Software: astropy (Astropy Collaboration et al. 2013), emcee (Foreman-Mackey et al. 2013)

REFERENCES

Armstrong, D. J., Pugh, C. E., Broomhall, A.-M., et al. 2016, MNRAS, 455, 3110

Arnold, B. C. 2015, Pareto Distributions, 2nd edn. (CRC Press, Boca Raton, FL)

Astropy Collaboration, Robitaille, T. P., Tollerud, E. J., et al. 2013, A&A, 558, A33

Benz, A. O., & Güdel, M. 2010, ARA&A, 48, 241

Berger, E., Basri, G., Gizis, J. E., et al. 2008, ApJ, 676, 1307

Berger, E., Basri, G., Fleming, T. A., et al. 2010, ApJ, 709, 332

Bochanski, J. J., West, A. A., Hawley, S. L., & Covey, K. R. 2007, AJ, 133, 531

Burgasser, A. J., & Mamajek, E. E. 2017, ApJ, 845, 110

Burgasser, A. J., Kirkpatrick, J. D., Brown, M. E., et al. 2002, ApJ, 564, 421

Chambers, K. C., Magnier, E. A., Metcalfe, N., et al. 2016, ArXiv e-prints, arXiv:1612.05560

Clauset, A., Shalizi, C. R., & Newman, M. E. J. 2009, ArXiv e-prints

Cruz, K. L., Reid, I. N., Liebert, J., Kirkpatrick, J. D., & Lowrance, P. J. 2003, AJ, 126, 2421

Davenport, J. R. A. 2016, ApJ, 829, 23

—. 2017, Research Notes of the American Astronomical Society, 1, 2

Davenport, J. R. A., Kipping, D. M., Sasselov, D., Matthews, J. M., & Cameron, C. 2016, ApJL, 829, L31

Davenport, J. R. A., Hawley, S. L., Hebb, L., et al. 2014, ApJ, 797, 122

Donati, J.-F., & Landstreet, J. D. 2009, ARA&A, 47, 333

Dupuy, T. J., & Liu, M. C. 2012, ApJS, 201, 19

Epchtein, N., de Batz, B., Capoani, L., et al. 1997, The Messenger, 87, 27

Faherty, J. K., Burgasser, A. J., Cruz, K. L., et al. 2009, AJ, 137, 1

Foreman-Mackey, D., Hogg, D. W., Lang, D., & Goodman, J. 2013, PASP, 125, 306

Gagné, J., Lafrenière, D., Doyon, R., Malo, L., & Artigau, É. 2015, ApJ, 798, 73

Gershberg, R. E. 1972, Ap&SS, 19, 75

—. 2005, Solar-Type Activity in Main-Sequence Stars, doi:10.1007/3-540-28243-2

Gershberg, R. E., & Shakhovskaia, N. I. 1983, Ap&SS, 95, 235

Giampapa, M. S., & Liebert, J. 1986, ApJ, 305, 784

Gilliland, R. L., Jenkins, J. M., Borucki, W. J., et al. 2010, ApJL, 713, L160

Gillon, M., Jehin, E., Lederer, S. M., et al. 2016, Nature, 533, 221

Gillon, M., Triaud, A. H. M. J., Demory, B.-O., et al. 2017, Nature, 542, 456

Gizis, J. E., Burgasser, A. J., Berger, E., et al. 2013, ApJ, 779, 172

Gizis, J. E., Monet, D. G., Reid, I. N., et al. 2000, AJ, 120, 1085

Gizis, J. E., Paudel, R. R., Mullan, D., et al. 2017a, ApJ, 845, 33

Gizis, J. E., Paudel, R. R., Schmidt, S. J., Williams, P. K. G., & Burgasser, A. J. 2017b, ApJ, 838, 22

Grenfell, J. L., Gebauer, S., v. Paris, P., Godolt, M., & Rauer, H. 2014, Planet. Space Sci., 98, 66

Handberg, R., & Lund, M. N. 2014, MNRAS, 445, 2698

Hawley, S. L., Davenport, J. R. A., Kowalski, A. F., et al. 2014, ApJ, 797, 121

Hawley, S. L., & Pettersen, B. R. 1991, ApJ, 378, 725

Henry, T. J., Subasavage, J. P., Brown, M. A., et al. 2004, AJ, 128, 2460

Hilton, E. J. 2011, PhD thesis, University of Washington

Hogg, D. W., Bovy, J., & Lang, D. 2010, ArXiv e-prints, arXiv:1008.4686

Howell, S. B., Sobeck, C., Haas, M., et al. 2014, PASP, 126, 398

James, D. J., Jardine, M. M., Jeffries, R. D., et al. 2000, MNRAS, 318, 1217

Jardine, M., & Unruh, Y. C. 1999, A&A, 346, 883

Jenkins, J. M., Caldwell, D. A., Chandrasekaran, H., et al. 2010, ApJL, 713, L120

Kirkpatrick, J. D., Reid, I. N., Liebert, J., et al. 1999, ApJ, 519, 802

Koch, D. G., Borucki, W. J., Basri, G., et al. 2010, ApJL, 713, L79

Koen, C. 2013, MNRAS, 428, 2824

Kowalski, A. F., Hawley, S. L., Carlsson, M., et al. 2015, SoPh, 290, 3487

Kowalski, A. F., Hawley, S. L., Hilton, E. J., et al. 2009, AJ, 138, 633

Kowalski, A. F., Hawley, S. L., Holtzman, J. A., Wisniewski, J. P., & Hilton, E. J. 2010, ApJL, 714, L98

Kurochka, L. N. 1987, Soviet Ast., 31, 231

Lacy, C. H., Moffett, T. J., & Evans, D. S. 1976, ApJS, 30, 85

Lee, K., Moon, Y.-J., & Nakariakov, V. M. 2016, ApJ, 831, 131

Luger, R., Sestovic, M., Kruse, E., et al. 2017, Nature Astronomy, 1, 0129

Lund, M. N., Handberg, R., Davies, G. R., Chaplin, W. J., & Jones, C. D. 2015, ApJ, 806, 30

Lurie, J. C., Davenport, J. R. A., Hawley, S. L., et al. 2015, ApJ, 800, 95

Maehara, H., Shibayama, T., Notsu, S., et al. 2012, Nature, 485, 478

Magnier, E. A., Schlafly, E. F., Finkbeiner, D. P., et al. 2016, ArXiv e-prints, arXiv:1612.05242

Martín, E. L., Cabrera, J., Martioli, E., Solano, E., & Tata, R. 2013, A&A, 555, A108

Martín, E. L., Delfosse, X., Basri, G., et al. 1999, AJ, 118, 2466

McKinney, W. 2010, in Proceedings of the 9th Python in Science Conference, ed. S. van der Walt & J. Millman, 51 – 56

Miller, C. J., Genovese, C., Nichol, R. C., et al. 2001, AJ, 122, 3492

Mohanty, S., Basri, G., Shu, F., Allard, F., & Chabrier, G. 2002, ApJ, 571, 469

Mullan, D. J. 2010, ApJ, 721, 1034

Mullan, D. J., & Paudel, R. R. 2018, ApJ, 854, 14

Notsu, Y., Shibayama, T., Maehara, H., et al. 2013, ApJ, 771, 127

Osten, R. A., Kowalski, A., Sahu, K., & Hawley, S. L. 2012, ApJ, 754, 4

Owen, J. E., & Mohanty, S. 2016, MNRAS, 459, 4088

Paudel, R. R., Gizis, J. E., Mullan, D., et al. 2018, in American Astronomical Society Meeting Abstracts, Vol. 231, American Astronomical Society Meeting Abstracts 231, 349.10

Pineda, J. S., Hallinan, G., & Kao, M. M. 2017, ApJ, 846, 75

Ramsay, G., Doyle, J. G., Hakala, P., et al. 2013, MNRAS, 434, 2451

Reid, I. N., Cruz, K. L., Kirkpatrick, J. D., et al. 2008, AJ, 136, 1290

Reiners, A., & Basri, G. 2008, ApJ, 684, 1390

Reiners, A., & Christensen, U. R. 2010, A&A, 522, A13

Roettenbacher, R. M., & Kane, S. R. 2017, ApJ, 851, 77

Route, M. 2016, ApJL, 830, L27

Route, M., & Wolszczan, A. 2012, ApJL, 747, L22

—. 2016, ApJ, 830, 85

Schmidt, S. J., Hawley, S. L., West, A. A., et al. 2015, AJ, 149, 158

Schmidt, S. J., West, A. A., Bochanski, J. J., Hawley, S. L., & Kielty, C. 2014, PASP, 126, 642

Schmidt, S. J., West, A. A., Hawley, S. L., & Pineda, J. S. 2010, AJ, 139, 1808

Schmidt, S. J., Shappee, B. J., Gagné, J., et al. 2016, ApJL, 828, L22

Schneider, A. C., Greco, J., Cushing, M. C., et al. 2016, ApJ, 817, 112

Segura, A., Walkowicz, L. M., Meadows, V., Kasting, J., & Hawley, S. 2010, Astrobiology, 10, 751

Shibayama, T., Maehara, H., Notsu, S., et al. 2013, ApJS, 209, 5

Stetson, P. B. 1996, PASP, 108, 851

Telleschi, A., Güdel, M., Briggs, K., et al. 2005, ApJ, 622, 653

Tilley, M. A., Segura, A., Meadows, V. S., Hawley, S., & Davenport, J. 2017, ArXiv e-prints, arXiv:1711.08484

Tonry, J. L., Stubbs, C. W., Lykke, K. R., et al. 2012, ApJ, 750, 99

Vida, K., Kővári, Z., Pál, A., Oláh, K., & Kriskovics, L. 2017, ApJ, 841, 124

Walkowicz, L. M., Basri, G., Batalha, N., et al. 2011, AJ, 141, 50

Weinberger, A. J., Boss, A. P., Keiser, S. A., et al. 2016, AJ, 152, 24

Welch, D. L., & Stetson, P. B. 1993, AJ, 105, 1813

Williams, P. K. G., & Berger, E. 2015, ApJ, 808, 189

Yadav, R. K., Christensen, U. R., Morin, J., et al. 2015, ApJL, 813, L31